High Capacity, Safety, and Enhanced Cyclability of Lithium Metal Battery Using a V_2O_5 Nanomaterial Cathode and Room Temperature Ionic Liquid Electrolyte

Shu-Lei Chou,*[,†,‡] Jia-Zhao Wang,[†,‡] Jia-Zeng Sun,[‡,§] David Wexler,[||] Maria Forsyth,[‡,§] Hua-Kun Liu,[†,‡] Douglas R. MacFarlane,[‡,⊥] and Shi-Xue Dou[†]

Institute for Superconducting and Electronic Materials and Faculty of Engineering, University of Wollongong, Wollongong, NSW 2522 Australia, Department of Materials Engineering and School of Chemistry, Monash University, Clayton, VIC 3800 Australia, and ARC Centre of Excellence for Electromaterials Science Australia

Received May 30, 2008. Revised Manuscript Received August 21, 2008

V_2O_5 nanomaterials including nanoribbons, nanowires, and microflakes have been synthesized by an ultrasonic assisted hydrothermal method and combined with a post-annealing process. The as-annealed V_2O_5 nanomaterials are characterized by X-ray diffraction (XRD), Brunauer−Emmett−Teller (BET) N_2 adsorption, scanning electron microscopy (SEM), transmission electron microscopy (TEM), and high resolution transmission electron microscopy (HRTEM). A room temperature ionic liquid (RTIL) has been used as an electrolyte ($[C_3mpyr][NTf_2]$ containing 1 M $LiNTf_2$) in rechargeable lithium metal batteries by combining V_2O_5 nanomaterials as cathode materials. The electrochemical tests including constant current charge−discharge, cyclic voltammetry (CV), and electrochemical impedance spectroscopy (EIS) show near theoretical specific capacity, improved cyclability, good high-rate capability, and enhanced kinetics. The thermogravimetric analysis (TGA) results show that the RTIL can prevent the dissolution of V_2O_5 during charge and discharge. The rechargeable lithium battery presented here using V_2O_5 nanoribbons as cathode materials and RTIL as electrolyte could be the next generation lithium battery with high capacity, safety, and long cycle life.

1. Introduction

The lithium metal battery is one of the most promising high-energy-density batteries due to the most negative potential of the Li/Li^+ couple and its high theoretical capacity (more than 3860 mA h g^{-1}).[1] To achieve a safe and practical high-energy-density rechargeable lithium battery requires selection of an optimum electrolyte and a compatible and high-capacity cathode material. Electrolyte materials currently used in lithium ion batteries present significant safety issues for lithium metal batteries due to the use of flammable organic electrolytes and the formation of lithium dendrites. Room temperature ionic liquid (RTIL), on the other hand are, in some cases, flame resistant, nonvolatile, electrochemical stable, and able to effectively prevent the formation of lithium dendrites, showing potential as safe electrolytes for use in lithium battery systems.[2−4] Among the large family of RTILs, pyrrolidinium bis(trifluoromethanesulfonyl) amide salts in particular show high cathodic stability against lithium metal, relatively high ion conductivity, nonflammability, and also good electrochemical properties in battery tests.[5−8] However, in many cases the ionic liquids which provide optimum performance on the Li anode do not work well with the typical lithium battery cathode materials, often producing poor cycle life. One of the goals of this work was to demonstrate an RTIL/cathode combination exhibiting good cycle life.

Among the known cathode materials of lithium metal batteries, vanadium pentoxide (V_2O_5) is one of the most promising, offering the advantages of low cost and high theoretical capacity (437 mA h g^{-1}) compared with typical commercial cathode materials, for example, $LiCoO_2$ (∼273 mA h g^{-1}).[9,10] Recently, nanostructured V_2O_5 including

* Corresponding author. E-mail: sc478@uow.edu.au.
† Institute for Superconducting and Electronic Materials, University of Wollongong.
‡ ARC Centre of Excellence for Electromaterials Science Australia.
§ Department of Materials Engineering, Monash University.
|| Faculty of Engineering, University of Wollongong.
⊥ School of Chemistry, Monash University.

(1) Reddy, T. B.; Hossain, S. In *Handbook of batteries*, 3rd ed.; Linden, D., Reddy, T. B., McGraw-Hill: New York, 2002; Chapter 34.
(2) Galinski, M.; Lewandowski, A.; Stepniak, I. *Electrochim. Acta* **2006**, *51*, 5567.
(3) MacFarlane, D. R.; Forsyth, M.; Howlett, P. C.; Pringle, J. M.; Sun, J. Z.; Annat, G.; Neil, W.; Izgorodina, E. I. *Acc. Chem. Res.* **2007**, *40*, 1165.
(4) Byrne, N.; Howlett, P. C.; MacFarlane, D. R.; Forsyth, M. *Adv. Mater.* **2005**, *17*, 2497.
(5) MacFarlane, D. R.; Meakin, P.; Sun, J.; Amini, N.; Forsyth, M. *J. Phys. Chem. B* **1999**, *103*, 4164.
(6) Sakaebe, H.; Matsumoto, H. *Electrochem. Commun.* **2003**, *5*, 594.
(7) Shin, J. H.; Henderson, W. A.; Passerini, S. *J. Electrochem. Soc.* **2005**, *152*, A978.
(8) Howlett, P. C.; Brack, N.; Hollenkamp, A. F.; Forsyth, M.; MacFarlane, D. R. *J. Electrochem. Soc.* **2006**, *153*, A595.
(9) (a) Winter, M.; Besenhard, J. O.; Spahr, M. E.; Novak, P. *Adv. Mater.* **1998**, *10*, 725. (b) Tan, K. S.; Reddy, M. V.; Subba Rao, G. V.; Chowdari, B. V. R. *J. Power Sources* **2005**, *147*, 241.
(10) Whittingham, M. S. *Chem. Rev.* **2004**, *104*, 4271.

10.1021/cm801468q CCC: $40.75
Published on Web 10/31/2008

nanotubes,[11−14] nanobelts,[15−18] nanorods,[19] and nanowires[20,21] has been extensively investigated to improve its electrochemical properties by creating short diffusion lengths for the Li^+ ions, a high contact surface area between the active materials and electrolyte, and a large flexibility for volume changes caused by Li^+ insertion/extraction.[22] However, limited cyclability remains the major problem of such electrode materials in most reports due to the decomposition of the electrolytes (especially the solvent) or the dissolution of the active material during the charge−discharge process.[23] Although some of the studies showed improved cyclability through doping, they suffered from lowered capacity.[24,25] In this paper, we report a novel porous V_2O_5 nanoribbon cathode material combined with an RTIL electrolyte showing safety, high specific capacity, good rate performance, and enhanced cyclability.

To synthesize nanostructured V_2O_5, a variety of methods, including sol−gel processing, template-based methods, thermal evaporation, hydrothermal/solvothermal synthesis, reverse micelle techniques, and electrochemical deposition, have been developed.[26−34] Among these methods, hydrothermal synthesis has to be considered the easiest and most effective way.[35] With the assistance of surfactants, different morphologies of V_2O_5 have been prepared by the hydrothermal method.[28,29,34] However, the processing time in hydrothermal treatment was normally 24 h or longer. Here, a new modified hydrothermal method with ultrasonic assistance for initial dispersion was introduced to reduce the processing time to 2 h.

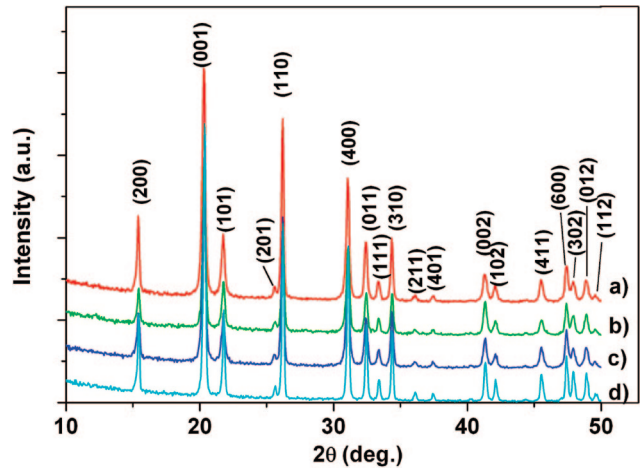

Figure 1. XRD patterns of V_2O_5 nanoribbons (a), nanowires (b), microflakes (c), and commercials powder (d).

2. Experimental Section

2.1. Synthesis. V_2O_5 nanomaterials were synthesized by the hydrothermal method with ultrasonic assistance for initial dispersion and followed by a post annealing process at 400 °C in air. First, commercial V_2O_5 powder (0.5 mmol) and the nonionic surfactant Brij 30 ($C_{12}H_{25}(OCH_2CH_2)_4OH$), 10 mmol in 30 mL deionized water using a total volume of 120 mL, in an autoclave were put into an ultrasonic bath for 20 min. Then, the autoclave was under hydrothermal treatment at 170 °C for 2 h to obtain as-prepared vanadium oxide nanoribbons. The as-obtained vanadium oxide nanostructures were washed three times in deionized water and three times in acetone, dried in a vacuum oven at 80 °C for 12 h, and finally annealed at 400 °C in air for 3 h. V_2O_5 nanowires were prepared by changing the surfactant into Triton X-100 (*t*-octylphenyl-$(OCH_2CH_2)_xOH$, $x = 9-10$) under the same condition. V_2O_5 microflakes were synthesized under the same condition without using surfactant.

2.2. Instrument Analysis. The morphology and microstructure of V_2O_5 nanomaterials were characterized by using X-ray diffraction (XRD) (Philips PW1730), scanning electron microscopy (SEM) (JEOL JEM-3000, 30 KV) equipped with energy dispersive X-ray spectroscopy (EDS), transmission electron microscopy (TEM) (JEOL 2011, 200 KV), Brunauer−Emmett−Teller (BET) (Quanta Chrome Nova 1000), and thermal gravimetric analysis (TGA) (TA 2000 Thermoanalyzer). To test the XRD for postcycling electrode, the cells were opened, and the electrodes were taken out, washed with DMC three times, and washed and soaked with acetone for 24 h in a glovebox. To test the TGA, after being washed, the electrodes were taken out from the glovebox and put into vacuum oven at 120 °C for 12 h. The composites including V_2O_5, acetylene black, and PVdF were peeled off from electrodes and put into small platinum bowls. The heating rate is 5 °C min^{-1}, and the heating range is 30 to 550 °C.

2.3. Electrochemical Characterizations. To test the electrochemical performance, V_2O_5 nanomaterials were mixed with acetylene black (AB) and a binder, polyvinylidene fluoride (PVdF), in a weight ratio of 70:20:10 in a solvent (*N*-methyl-2-pyrrolidone). The slurry was uniformly pasted onto pieces of Al foil with an area of 1 cm^2. Such prepared electrode sheets were dried at 120

(11) Spahr, M. E.; Stoschitzki-Bitterli, P.; Nesper, R.; Haas, O.; Novak, P. *J. Electrochem. Soc.* **1999**, *146*, 2780.
(12) Lutta, S. T.; Dong, H.; Zavalij, P. Y.; Whittingham, M. S. *Mater. Res. Bull.* **2005**, *40*, 383.
(13) Wang, Y.; Takahashi, K.; Shang, H.; Cao, G. Z. *J. Phys. Chem. B* **2005**, *109*, 3085.
(14) Li, H. X.; Jiao, L. F.; Yuan, H. T.; Zhang, M.; Guo, J.; Wang, L. Q.; Zhao, M.; Wang, Y. M. *Electrochem. Commun.* **2006**, *8*, 1693.
(15) Li, G. C.; Pang, S. P.; Jiang, L.; Guo, Z. Y.; Zhang, Z. K. *J. Phys. Chem. B* **2006**, *110*, 9383.
(16) Li, B. X.; Xu, Y.; Rong, G. X.; Jing, M.; Xie, Y. *Nanotechnology* **2006**, *17*, 2560.
(17) Chan, C. K.; Peng, H. L.; Twesten, R. D.; Jarausch, K.; Zhang, X. F.; Cui, Y. *Nano Lett.* **2007**, *7*, 490.
(18) Shi, S. F.; Cao, M. H.; He, X. Y.; Xie, H. M. *Cryst. Growth Des.* **2007**, *7*, 1893.
(19) Cao, A. M.; Hu, J. S.; Liang, H. P.; Wan, L. J. *Angew. Chem., Int. Ed.* **2005**, *44*, 4391.
(20) Patrissi, C. J.; Martin, C. R. *J. Electrochem. Soc.* **1999**, *146*, 3176.
(21) Li, X. X.; Li, W. Y.; Ma, H.; Chen, J. *J. Electrochem. Soc.* **2007**, *154*, A39.
(22) Wang, Y.; Cao, G. Z. *Chem. Mater.* **2006**, *18*, 2787.
(23) Aurbach, D.; Goffer, Y. In *Nonaqueous Electrochemistry*; Aurbach, D., Ed.; Marcel Dekker Inc.: New York, 1999; Chapter 4.
(24) Coustier, F.; Hill, J.; Owens, B. B.; Passerini, S.; Smyrl, W. H. *J. Electrochem. Soc.* **1999**, *146*, 1355.
(25) Dobley, A.; Ngalas, K.; Yang, S.; Zavalij, P. Y.; Whittingham, M. S. *Chem. Mater.* **2001**, *13*, 4382.
(26) Livage, J. *Chem. Mater.* **1991**, *3*, 578.
(27) Ajayan, P. M.; Stephan, O.; Redlich, P.; Colliex, C. *Nature* **1995**, *375*, 564.
(28) Spahr, M. E.; Bitterli, P.; Nesper, R.; Müller, M.; Krumeich, F.; Nissen, H. U. *Angew. Chem., Int. Ed.* **1998**, *37*, 1263.
(29) Muhr, H. J.; Krumeich, F.; SchPnholzer, U. P.; Bieri, F.; Niederberger, M.; Gauckler, L. J.; Nesper, R. *Adv. Mater.* **2000**, *12*, 231.
(30) Liu, P.; Lee, S. H.; Tracy, C. E.; Yan, Y.; Turner, J. A. *Adv. Mater.* **2002**, *14*, 27.
(31) Gu, G.; Schmid, M.; Chiu, P. W.; Minett, A.; Fraysse, J.; Kim, G. T.; Roth, S.; Kozlov, M.; Munoz, E.; Baughman, R. H. *Nat. Mater.* **2003**, *2*, 316.
(32) Pinna, N.; Wild, U.; Urban, J.; SchlPgl, R. *Adv. Mater.* **2003**, *15*, 329.
(33) Takahashi, K.; Limmer, S. J.; Wang, Y.; Cao, G. *J. Phys. Chem. B* **2004**, *108*, 9795.
(34) Liu, J.; Wang, X.; Peng, Q.; Li, Y. *Adv. Mater.* **2005**, *17*, 764.
(35) Chirayil, T.; Zavalij, P. Y.; Whittingham, M. S. *Chem. Mater.* **1998**, *10*, 2629.

Table 1. Specific Surface Areas, Lattice Parameters, and Crystal Sizes of V_2O_5 Nanoribbons, Nanowires, Microflakes, and Commercial Powder

		sample			
		nanoribbons	nanowires	microflakes	commercial powder
surfactant		Brij 30	Triton 100	N/A	N/A
Hydrothermal treatment time (h)		2	2	2	N/A
BET (m^2 g^{-1})	as-prepared	39.5	22.8	14.5	5.7
	annealed at 400 °C	31	15	9.2	N/A
lattice parameters	*a* (Å)	11.5100	11.5085	11.5085	11.5076
	b (Å)	3.5625	3.5614	3.5609	3.5589
	c (Å)	4.3717	4.3707	4.3690	4.3670
	volume (Å^3)	179.3	179.1	179.0	178.8
crystal size (nm)		62.2	93.4	112.1	420.2

°C in a vacuum oven and pressed under a pressure of approximately 3000 kg cm^{-2} for 10 s. Electrochemical measurements, including charge−discharge, cyclic voltammetry (CV), and electrochemical impedance spectroscopy (EIS) were performed using a Neware battery tester and a CHI 660b electrochemistry workstation, respectively. The electrochemical cell (CR 2032 coin-type cell) contained V_2O_5 nanomaterials on an Al foil as the working electrode, a Li foil as the counter electrode and reference electrode, a porous polypropylene film as separator, and 1 M lithium bis(trifluoromethanesulfonyl)imide ($LiNTf_2$) in *N*-methyl-*N*-propyl pyrrolidinium bis(trifluoromethanesulfonyl) imide ($[C_3mpyr][NTf_2]$) ionic liquid as the electrolyte. $[C_3mpyr][NTf_2]$ was prepared as previously reported.[5] The commercial electrolyte used was 1 M $LiPF_6$ in a 50:50 (v/v) mixture of ethylene carbonate (EC) and dimethyl carbonate (DMC) obtained from MERCK KgaA, Germany.

3. Results and Discussion

3.1. Structural and Morphological Analysis. *3.1.1. XRD and BET.* V_2O_5 nanoribbons, nanowires, and microflakes were prepared by hydrothermal treatment of ultrasonically suspended commercial V_2O_5 powder in an aqueous surfactant (Brij 30, or Triton 100) solution, followed by a post-annealing process in air. Ultrasonic treatment could cause commercial V_2O_5 to effectively form a homogeneous suspension in the solution, and the reaction time of hydrothermal treatment could be shortened. X-ray diffraction (XRD) measurement was used to study the phase of as-annealed V_2O_5 nanomaterials (Figure 1). The diffraction peaks of the XRD patterns for all the samples can be indexed to an orthorhombic phase of V_2O_5 (JCPDS no. 41-1426). No peaks of any other phases were detected, indicating the high purity of V_2O_5 structures. The lattice parameters are listed in Table 1. The values of lattice parameters including *a*, *b*, and *c* and the cell volume tend to show the order of nanoribbons > nanowires > microflakes > commercial powder. It is believed that the higher the value of *a*, the bigger the interlayer distance will be, and mobility and distribution of lithium ions between layers can be improved. Therefore, the nanoribbons show the best mobility of lithium ions. The crystal sizes of V_2O_5 nanoribbons, nanowires, microflakes, and commercial powder using the Debye−Scherrer equation applied to the (002) peaks are listed in Table 1. It can be seen that nanoribbons have the smallest crystal size (62.2 nm), which is much smaller than that of the commercial powder (420.2 nm). The crystal sizes of V_2O_5 nanomaterials follow the order of nanoribbons < nanowires < microflakes < commercial powder. The specific surface areas of as-prepared and after annealed products were measured by 15 points Brunauer−Emmett−Teller (BET) N_2 adsorption method shown in Table 1. The specific surface areas of nanomaterials are all dropped compared with as-prepared products due to the annealing process. The V_2O_5 nanoribbons show the highest specific surface area (31.0 m^2 g^{-1}), while the commercial powder only has a surface area of 5.7 m^2 g^{-1}. The surface areas follow the trend of nanoribbons > nanowires > microflakes > commercial powder. It can be found that the smaller crystal size shows the higher surface area.

3.1.2. SEM and TEM. Typical scanning electron microscopy (SEM) and transmission electron microscopy (TEM) images of the V_2O_5 nanoribbons, nanowires, and microflakes are shown in Figure 2. Figure 2a shows bundles of nanoribbons of about 5 μm in length, 500 nm in width, and approximately 20 nm in thickness. Figure 2b displays V_2O_5 nanowires of almost 20 μm length and 50−300 nm in diameter. In Figure 2c, round and square V_2O_5 microflakes can be seen over a large area with thickness of ~2 μm and diameter of ~10 μm. Further TEM observations are shown in Figure 2d,e for nanoribbons and Figure 2f,g for nanowires. It can be seen that the nanoribbons were composed of small nanoflakes (Figure 2d and Supporting Information Figure S2a), and the high resolution TEM (HRTEM) image taken from the edge of a nanoflakes (Figure 2e) demonstrates that the nanoparticle has a porous structure on the surface with diameters less than 5 nm (Supporting Information Figure S2b), which might also account for the high surface area. The possible reason for the formation of the pores is that the surfactant (Brij 30) could etch the surface of the raw V_2O_5 materials, and show a surface porous structure after annealing. The lattice fringes are visible with a spacing of 0.58 nm, which is in good agreement with the spacing of the (200) planes of V_2O_5. The TEM image in Figure 2f affirms the nanowire-like morphology with a smooth surface. The HRTEM image (Figure 2g) shows clear lattice fringes with a spacing of 0.58 nm, matching the (200) spacing of V_2O_5. Since the hydrothermal treatment time is very short (2 h), the nanowires and nanoflakes were not single crystal. Different crystalline orientations were found during the TEM analysis.

3.2. Electrochemical Characterization. *3.2.1. Charge and Discharge Curves.* Figure 3 shows the charge−discharge curves of V_2O_5 nanoribbon electrodes in coin test cells using RTIL electrolyte and conventional electrolyte at a current density of 0.1 C. Here, *N*-methyl-*N*-propyl pyrrolidinium bis(trifluoromethanesulfonyl) imide ($[C_3mpyr][NTf_2]$) containing 1 M lithium bis(trifluoromethanesulfonyl)imide ($LiNTf_2$) was chosen as the RTIL electrolyte. Three discharge

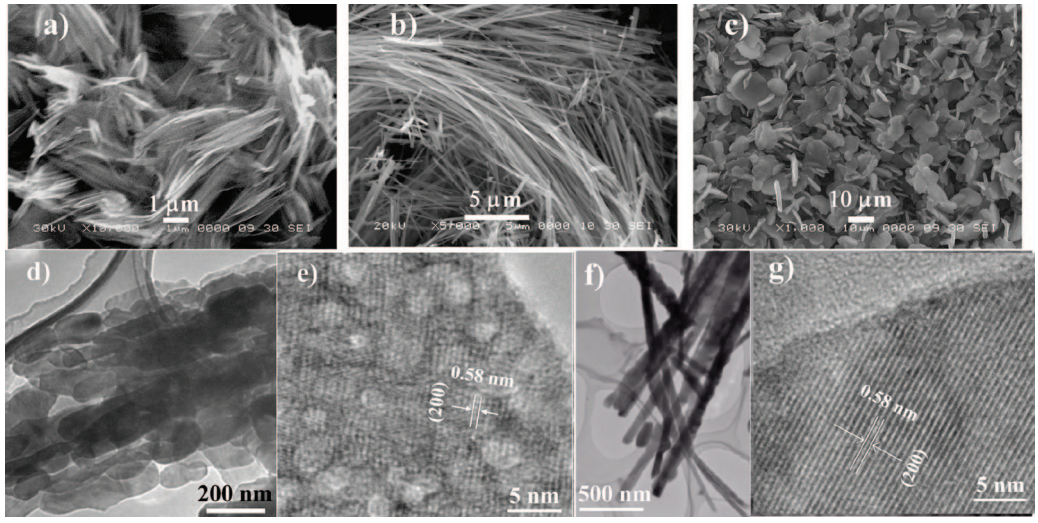

Figure 2. SEM images of (a) nanoribbons, (b) nanowires, and (c) microflakes; TEM and HRTEM images of (d, e) nanoribbons and (f, g) nanowires.

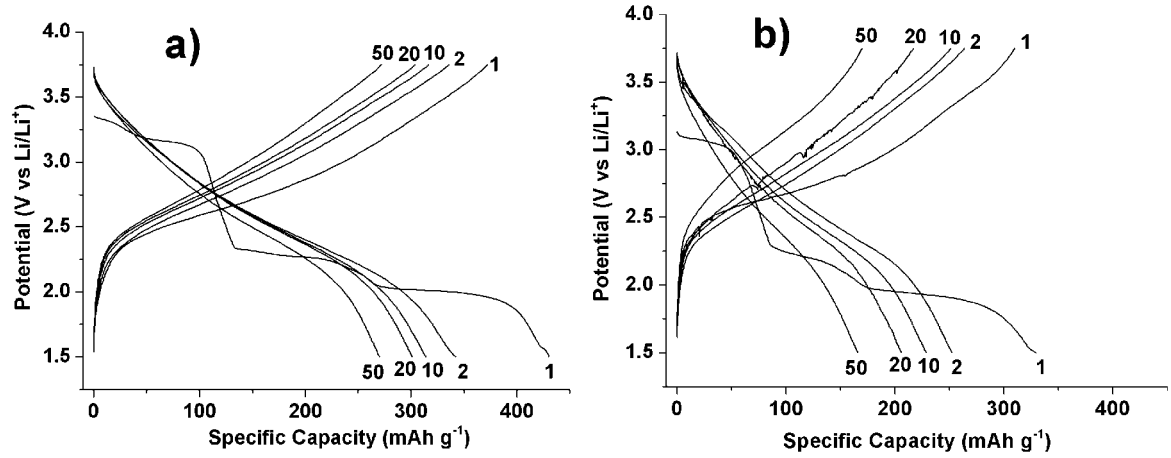

Figure 3. Typical charge−discharge curves for V_2O_5 nanoribbon in (a) RTIL electrolyte and (b) conventional electrolyte at current density of 0.1 C (C = 437 mA g^{-1}) at 25 °C.

plateaus for the initial discharges were observed for both electrolytes, showing the similar reaction mechanism for Li^+ ion intercalation into the V_2O_5. The known successive phase transformations on lithium ion insertion and extraction,[36,37] via α-$Li_xV_2O_5$ ($x < 0.01$), ε-$Li_xV_2O_5$ ($0.35 < x < 0.7$), δ-$Li_xV_2O_5$ ($x = 1$), γ-$Li_xV_2O_5$ ($1 < x < 3$), and ω-$Li_xV_2O_5$ ($x = 3$) can be clearly observed in the RTIL electrolyte. The nanoribbon electrode in RTIL electrolyte shows higher discharge plateau potentials than in conventional electrolyte because the RTIL electrolyte can more effectively prevent the self-discharge than conventional electrolyte. It is noticed that the open circuit potentials of RTIL batteries are almost the same (3.36 V), while those of conventional electrolyte batteries are lower and varied a lot. The initial discharge specific capacities for the nanoribbons in RTIL and conventional electrolyte are 430 and 329 mA h g^{-1}, respectively. The nanoribbon electrode in RTIL electrolyte shows close to the theoretical specific capacity (437 mA h g^{-1}, corresponding to 3 mol Li^+ ion). This observation reflects both the structure of the nanoribbons formed as a porous assembly of small nanoflakes, which provides short Li^+ ion diffusion lengths and high surface active position,[38] and the RTIL electrolyte which has the better electrochemical stability and which may also prevent the dissolution of (or reaction with) V_2O_5. For the second cycle, the specific capacities are 342 and 252 mA h g^{-1} in RTIL and conventional electrolyte, respectively. The large irreversible capacity is mainly due to the irreversible phase transformation. The V_2O_5 becomes amorphous after the initial discharge as the charge and discharge curves after initial discharge are similar as the amorphous V_2O_5 behavior in a previous report.[39,40] Moreover, the XRD analysis (Supporting Information Figure S3) performed on the electrode after 50 cycles shows the amorphous structure of V_2O_5 nanoribbons in both RTIL and conventional electrolyte. After 50 cycles, the nanoribbon electrode in RTIL electrolyte shows capacity of 270 mA h g^{-1}, while the nanoribbon electrode in conventional electrolytes only shows 182 mA h g^{-1} under 0.1 C, the latter being similar to results reported for 1D-nanostructured

(36) Delmas, C.; Brethes, S.; Menetrier, M. *J. Power Sources* **1991**, *34*, 113.
(37) Delmas, C.; Cognac-Auradou, H.; Cocciantelli, J. M.; Menetrier, M.; Doumerc, J. P. *Solid State Ionics* **1994**, *69*, 257.
(38) Fu, R. Q.; Ma, Z. R.; Zheng, J. P.; Au, G.; Plichta, E. J.; Ye, C. H. *J. Phys. Chem. B* **2003**, *107*, 9730.
(39) Machida, N.; Fuchida, R.; Minami, T. *J. Electrochem. Soc.* **1989**, *136*, 2133.
(40) Nabavi, M.; Sanchez, C.; Taulelle, F.; Livage, J. *Solid State Ionics* **1988**, *28*, 1183.

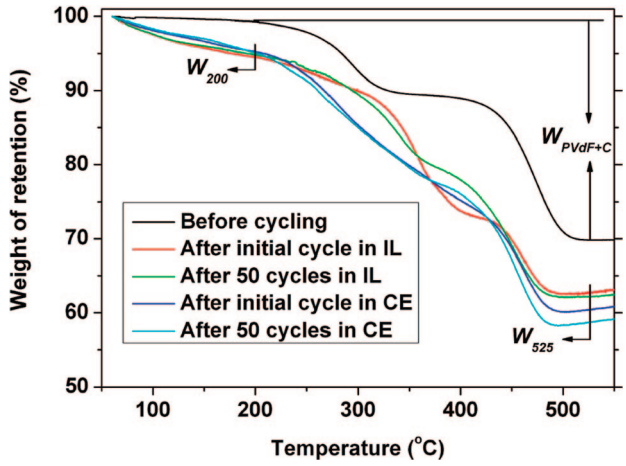

Figure 4. TGA curves of V_2O_5 nanoribbon electrodes in RTIL and conventional electrolyte (CE) after initial cycle and 50 cycles in fully charged state, respectively.

Table 2. TGA Result of the V_2O_5 Nanoribbon Electrodes in RTIL and Conventional Electrolyte (CE) after Initial Cycle and 50 Cycles in Fully Charged State, Respectively

cycle state	electrolyte	total mass loss (W_{TL}, %)	V_2O_5 loss (W_{VL}, %)
before cycle	N/A	30.24 = W_{PVdF+C}	none
after initial cycle	IL	33.86	10.70
after 50 cycles	IL	34.63	12.67
after initial cycle	CE	36.93	18.12
after 50 cycles	CE	38.77	22.01

V_2O_5.[22] It is also noticed that other morphologies of V_2O_5 including nanowires, microflakes, and commercial powder all show better cyclabilities in RTIL electrolytes than in conventional electrolytes.

3.2.2. Possible Reason for Enhanced Cyclability. After 50 cycles, the color of the separator in the cell using conventional electrolyte (Supporting Information Figure S4b) became yellow, while the color of the separator in RTIL electrolyte (Supporting Information Figure S4a) was still white. The EDS spectrum (Supporting Information Figure S5) which was taken from the separator with yellow materials confirmed the presence of vanadium element, indicating the loss of V_2O_5 in conventional electrolyte. The morphology of nanoribbon electrode in RTIL (Supporting Information Figure S6a) after 50 cycles still shows nanoflake-like structure which nanoribbons are composed of, while the morphology of nanoribbon electrode in conventional electrolyte (Supporting Information Figure S6b) after 50 cycles displays a much smoother surface indicating the loss of V_2O_5. To semiquantitatively measure the electrode weight loss in both RTIL and conventional electrolyte, thermal gravimetric analysis (TGA) was used to test the remaining V_2O_5 weight after the initial cycle and 50 cycles in the fully charged state as shown in Figure 4. The total-weight loss (W_{TL}, %) due to the decomposition of acetylene black and PVdF from 200 °C (W_{200}) to 525 °C (W_{525}) in air was calculated relative to the weight percentage at 200 °C using Equation 1. The weight loss of V_2O_5 (W_{VL}) was calculated by assuming that the total weight of acetylene black and PVdF was constant and that the Li-ion can ideally intercalate and deintercalate from V_2O_5 using eq 2, where W_{PVdF+C} (%) is the pristine percentage of PVdF and carbon in the electrode. The calculated data is listed in Table 2.

$$W_{TL} = \frac{W_{525} - W_{200}}{W_{200}} \quad (1)$$

$$W_{VL} = \left(1 - \frac{W_{PVdF+C}}{W_{TL}}\right) \times 100 \quad (2)$$

It can be seen that the V_2O_5 nanoribbon electrode lost more than 20% of its weight after the initial cycle in the conventional electrolyte, while it only lost 10% in the RTIL electrolyte. This means that the V_2O_5 nanoribbon electrode in the conventional electrolyte can only show 80% of theoretical capacity in the initial discharge, which is approximately 350 mA h g^{-1}, in good agreement with the charge−discharge result. After 50 cycles, the mass loss of V_2O_5 in conventional electrolyte is twice higher than that of the RTIL electrolyte, which is also confirmed with the cyclability curves (Figure 6), indicating how much more stable the nanostructured V_2O_5/RTIL electrolyte combination is. TGA results also show that the electrode materials including V_2O_5, PVdF, and active carbon are stable below 200 °C indicating the good thermal stability.[41] In addition, the RTIL electrolyte can also prevent the corrosion of Al by $LiNTf_2$,[42] which is a major obstacle to the use of $LiNTf_2$ salt electrolytes in practical lithium batteries.

3.2.3. Cyclic Voltammetry (CV). The electrochemical behaviors of different morphologies V_2O_5 using RTIL as electrolytes were further characterized by cyclic voltammograms (CV) shown in Figure 5. The initial negative scan occurs in mainly three steps indicating that in total 3 mol of Li ions reacts with 1 mol of V_2O_5. After the first negative scan, the reduction peak and oxidation peak only show one broad peak, respectively, indicating the irreversible phase transformation during the process of lithium ions insertion and extraction in the initial cycle. Since the different electrolytes and different scan rates are used here, the cyclic voltammograms of V_2O_5 commercial powder are slightly different from those in the references.[36,37,43] The use of RTILs as electrolyte could form a different solid state interface (SEI) layer with V_2O_5, which could also affect the CV results. The compatible and stable SEI layer might be another reason why V_2O_5 in RTIL electrolytes shows higher electrochemical performance than those in conventional electrolytes. The potentials and current densities of peaks are listed in Table 3. The potentials of the peaks for different morphologies are all similar showing the similar reaction mechanism. Nanoribbon and nanowire electrodes show much higher current densities than microflake and commercial powder V_2O_5 electrode, indicating the higher electrochemical activities of nanoribbon and nanowire electrodes. Small reduction peaks can still be seen in the second negative scan of the microflake and commercial powder electrodes. That

(41) (a) Maleki, H.; Deng, G. P.; Anani, A.; Howard, J. *J. Electrochem. Soc.* **1999**, *146*, 3224. (b) Reddy, M. V.; Subba Rao, G. V.; Chowdari, B. V. R. *J. Power Sources* **2006**, *159*, 263.
(42) Peng, C. X.; Yang, L.; Zhang, Z. X.; Tachibana, K.; Yang, Y. *J. Power Sources* **2007**, *173*, 510.
(43) Murugan, A. V.; Reddy, M. V.; Campet, G.; Vijayamohanan, K. *J. Electroanal. Chem.* **2007**, *603*, 287.

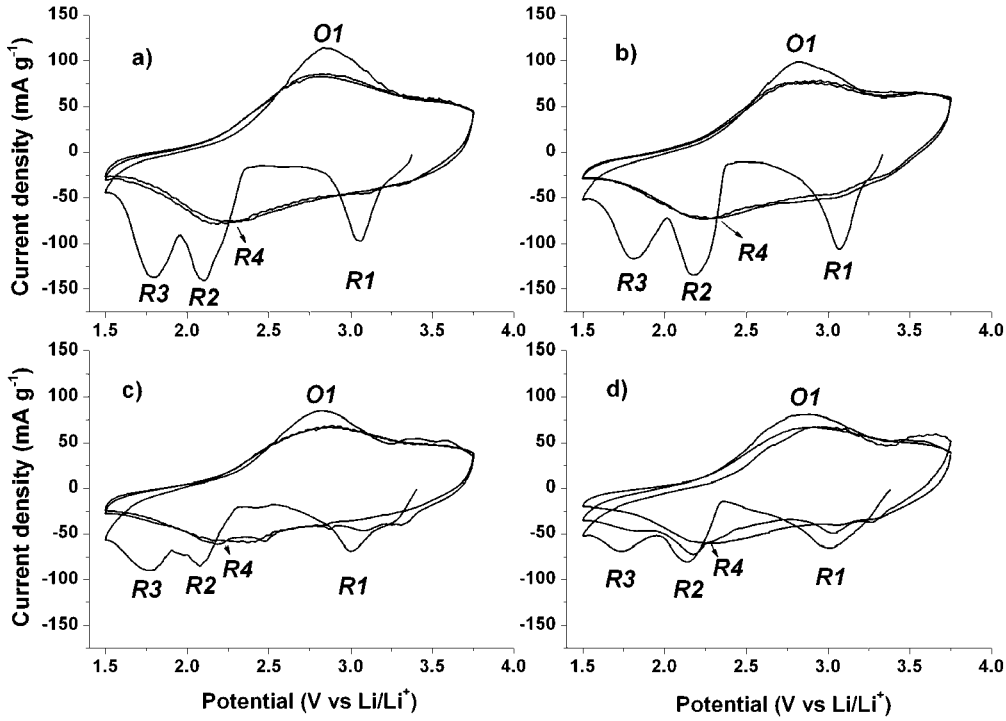

Figure 5. Cyclic voltammograms of V_2O_5 nanoribbon (a), nanowire (b), microflake (c), and commercials powder (d) electrode at scan rate of 0.1 mV s^{-1} using RTIL as electrolytes at 25 °C.

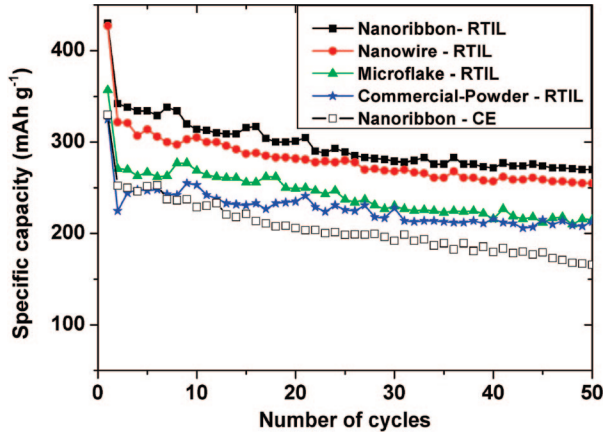

Figure 6. Cycle life of V_2O_5 nanoribbon (solid squares), nanowire (solid circles), microflake (solid triangles), and commercial-powder (solid stars) electrode using RTIL as electrolytes; V_2O_5 nanoribbon electrode using conventional electrolytes (hollow square) at 25 °C. Current densities are all 0.1 C (C = 437 mA h g^{-1}).

Table 3. Reduction Potentials E_{R1}, E_{R2}, E_{R3}, and E_{R4}, Oxidation Potential E_{O1}, and Current Density I_{R1}, I_{R2}, I_{R3}, I_{R4}, and I_{O1} for the V_2O_5 Nanoribbon, Nanowire, and Microflake and Commerical-Powder Electrodes at Scan Rate of 0.1 mV s^{-1} at 25 °C

	Potential (V vs Li/Li$^+$)					Current density (mA g^{-1})				
electrode	E_{R1}	E_{R2}	E_{R3}	E_{R4}	E_{O1}	I_{R1}	I_{R2}	I_{R3}	I_{R4}	I_{O1}
nanoribbons	3.05	2.10	1.79	2.23	2.84	97	140	138	77	114
nanowires	3.07	2.18	1.81	2.25	2.82	106	134	116	72	98
microflakes	3.00	2.07	1.78	2.22	2.83	68	84	89	61	85
commercial powder	3.02	2.14	1.74	2.26	2.86	65	80	68	60	81

is probably because nonreacted V_2O_5 (for the initial cycle) reacts with Li^+ ion in the following cycles due to the long Li^+ ion diffusion path arising from the large particle size and low surface area. Therefore, the capacities and rate performance of microflake and commercial powder electrodes would be much lower than nanoribbon and nanowire electrodes.

3.2.4. Cyclability. The cyclabilities of different V_2O_5 morphologies are shown in Figure 6. The initial discharge specific capacities for nanoribbon, nanowire, microflake, and commercial-powder electrodes are 430, 427, 347, and 255 mA h g^{-1}, respectively (Supporting Information Figure S7). The nanoribbon electrode shows the best retention of specific capacity, which may be due to the structure of nanoribbons formed by porous nanoflakes, which offer the short Li^+ ion diffusion lengths (small nanoflakes), high surface contact with electrolyte (high surface area), and the extra active position (surface pores). The slightly undulate curves of cyclability may be caused by the electrochemical activation process of the active materials in the first several cycles. After 50 cycles, the specific capacities follow the order of nanoribbons > nanowires > microflakes > commercial powder. The average Coulombic efficiencies are approximately 98%, 96%, 95%, and 93% for nanoribbons, nanowires, microflakes, and commercial powder in RTIL electrolytes, indicating the potential for industry application.

3.2.5. High-Rate Capability. Different rates of charge−discharge were also used to investigate the electrochemical performance of different morphologies in the RTIL electrolytes as shown in Figure 7a. It can be found that the high rate performance follows the order of nanoribbons > nanowires > microflakes > commercial powder. The V_2O_5 nanoribbon electrodes show the highest specific capacity of 119 mA h g^{-1} at a current density of 2 C. Changing rates of charge−discharge were also used for characterizing the stability of the nanoribbon electrode as shown in Figure 7b. There is only less than 5% capacity lost after changing the

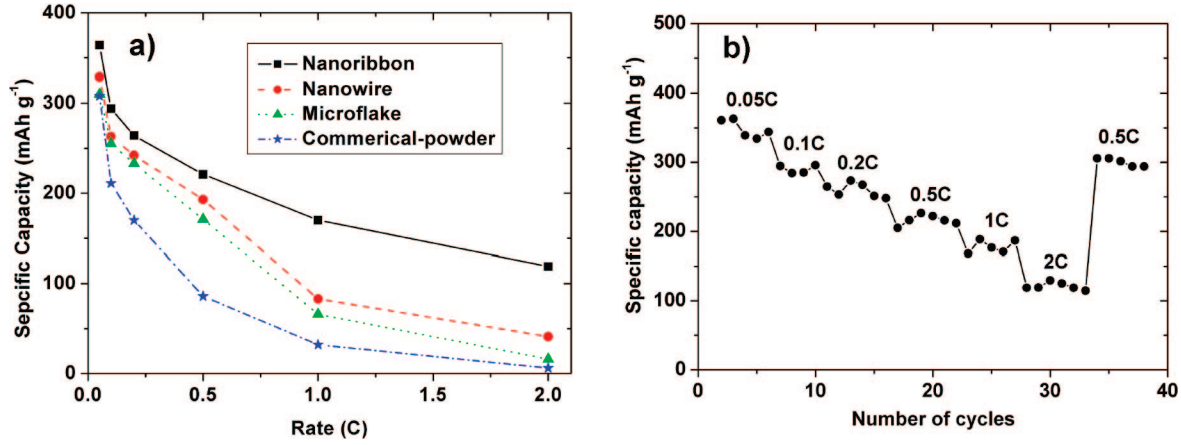

Figure 7. (a) Specific capacities of V_2O_5 nanoribbon (solid squares), nanowire (solid circles), microflake (solid triangles), and commercial-powder (solid stars) electrodes at different current densities using RTIL as electrolytes at 25 °C; (b) cycle life of V_2O_5 nanoribbon electrode using RTIL as electrolytes at changing current densities from 0.05 to 2 C and back to 0.05 C ($C = 437$ mA h g^{-1}) between 1.5 and 3.75 V vs Li/Li^+ at 25 °C.

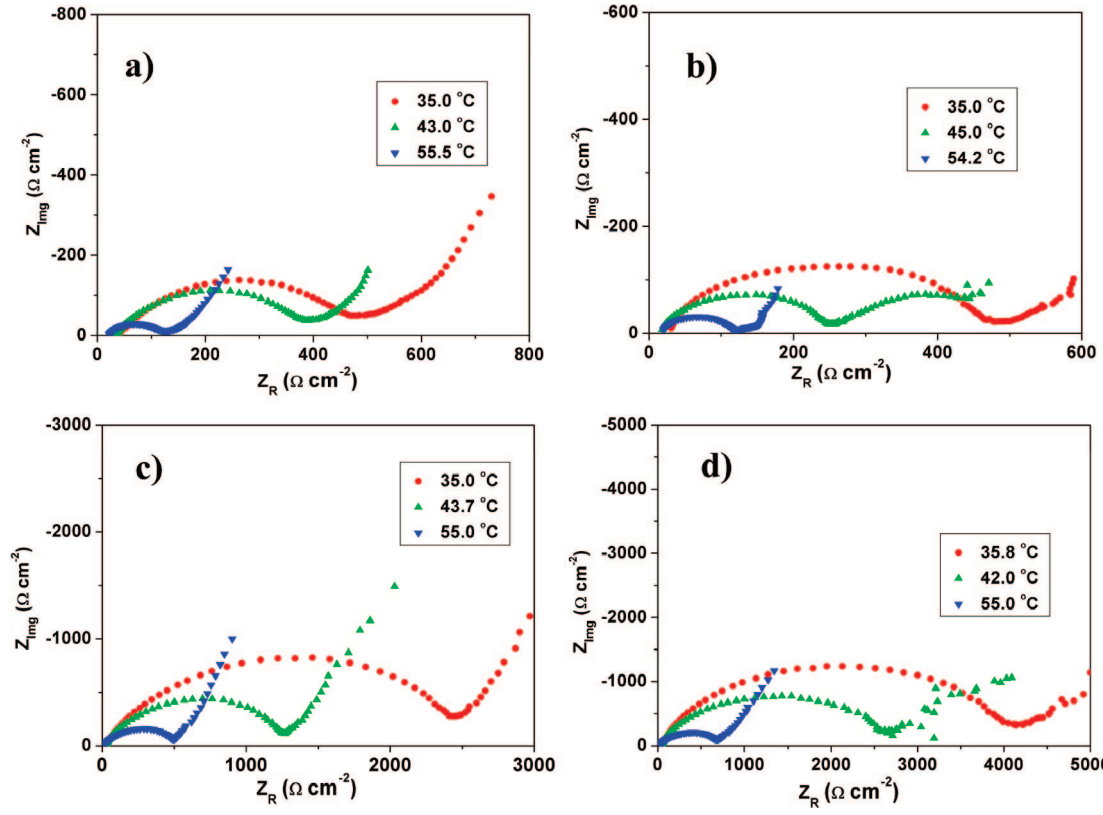

Figure 8. Nyquist plots of V_2O_5 nanoribbon (a), nanowire (b), microflake (c), and commercial powder (d) electrodes at a discharged potential of 3.0 V (vs Li/Li^+) at different temperatures from 100 kHz to 10 mHz.

current density from 0.05 to 2 C, and back to 0.05 C in 40 cycles, again showing the good stability of the nanoribbon electrode in the RTIL electrolyte.

3.2.6. Kinetics Investigation. To investigate the electrode kinetics, the apparent activation energies of V_2O_5 nanoribbon, nanowire, microflake, and commercial powder electrodes were calculated from electrochemical impedance spectra (EIS) using a previously reported method.[44,45] Figure 8 shows the Nyquist plots of the different morphologies of V_2O_5 electrodes at a discharged potential of 3.0 V vs Li/Li^+ at different temperatures after charge−discharge for five cycles. It can be found that the impedance curves show one compressed semicircle in the medium-frequency region which could be assigned to charge-transfer resistance (R_{ct}) and an approximately 45° inclined line in the low-frequency range which could be considered as Warburg impedance. The R_{ct} is calculated using the equivalent circuit shown in Figure S8 (Supporting Information). The exchange currents (i_0) and the apparent activation energies (E_a) for the lithium intercalated into V_2O_5 can be calculated from eq 3 and the Arrhenius equation (eq 4), respectively.

$$i_0 = RT/nFR_{ct} \tag{3}$$

$$i_0 = A \exp(-E_a/RT) \tag{4}$$

where A is a temperature-independent coefficient, R is the gas constant, T (K) is the absolute temperature, n is the

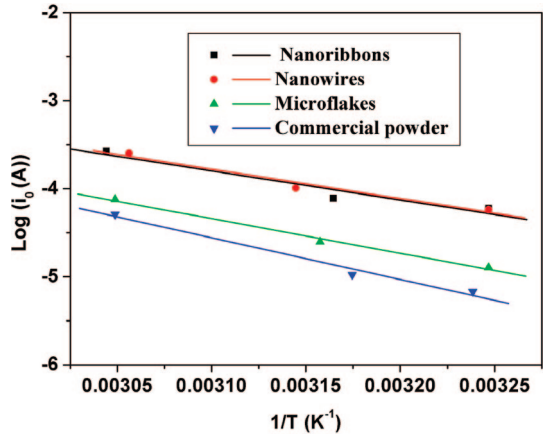

Figure 9. Arrhenius plots of log i_0 versus $1/T$ for the electrodes of V_2O_5 nanoribbon (black), nanowire (red), microflake (green), and commercial powder (blue) electrodes at a discharged potential of 3.0 V (vs Li/Li^+). The lines are the linear fitting results.

number of transferred electrons, and F is the Faraday constant. The values of R_{ct} and i_0 for different morphologies of V_2O_5 at different temperatures are summarized in Table S1 (Supporting Information). Figure 9 shows the Arrhenius plots of log i_0 as a function of $1/T$. The activation energies ($E_a = -Rk \ln 10$, k = the slope of the fitting line in Figure 9) of V_2O_5 nanoribbon, nanowire, microflake, and commercial powder electrodes at 3.0 V are calculated to be 63.3, 63.8, 75.3, and 90.7 kJ mol^{-1}, respectively. The apparent activation energies are in the order of nanoribbons < nanowires < microflakes < commercial powder. It is noticed that the V_2O_5 nanoribbon electrode shows the lowest activation energy which indicates the shortest lithium-ion diffusion path.[45] This enhanced kinetics could be explained as follows: the nanoribbons composed of porous nanoflakes show the highest surface area and thus provide the best penetration of the electrolyte as well as the shortest lithium diffusion length. Therefore, the nanoribbon electrode shows the best discharge capacity and best high-rate capability compared to other morphologies.

(44) Barsoukov, E.; Macdonald, J. R. *Impedance Spectroscopy Theory, Experiment, and Applications*; John Wiley & Sons: New York, 2005.
(45) Ma, H.; Zhang, S. Y.; Ji, W. Q.; Tao, Z. L.; Chen, J. *J. Am. Chem. Soc.* **2008**, *130*, 5361.

4. Conclusions

V_2O_5 nanomaterials were prepared by an ultrasonic assisted hydrothermal method followed by a post annealing process. The V_2O_5 nanoribbons with dimensions of about 5 μm in length, 500 nm in width, and approximately 20 nm in thickness show the highest capacity of 430 mA h g^{-1} for initial discharge, the best cyclability (270 mA h g^{-1} for the 50th cycle), good high-rate capability (119 mA h g^{-1} at 2 C current density), and enhanced kinetics in RTIL electrolytes. The TGA results show that the RTIL can prevent the dissolution of V_2O_5 during charge and discharge. The rechargeable lithium battery presented here using V_2O_5 nanoribbons as cathode materials and RTIL ($[C_3mpyr][NTf_2]$ containing 1 M $LiNTf_2$) as electrolyte could be the next generation lithium battery with high capacity, safety, and long cycle life.

Acknowledgment. Financial support provided by the Australian Research Council (ARC) through the ARC Centre of Excellence funding (CE0561616) is gratefully acknowledged. The authors also thank Dr. Tania Silver at the University of Wollongong for critical reading of the manuscript.

Supporting Information Available: SEM image of commercial V_2O_5 Powder, TEM images of V_2O_5 nanoribbons, XRD patterns of before and after cycling electrodes, pictures of separators taken out of cells in RTIL and conventional electrolyte after 50 cycles, EDS spectrum, SEM images of V_2O_5 nanoribbon electrodes in RTIL and conventional electrolyte after 50 cycles, charge−discharge curves of V_2O_5 nanowires, microflakes, and commercial powder in RTIL electrolyte, equivalent circuit, and the table of calculated R_{ct} and i_0 (PDF). This information is available free of charge via the Internet at http://pubs.acs.org.

CM801468Q